Synergistic Combination of Plasma Sputtered Pd-Au Bimetallic Nanoparticles for Catalytic Methane Combustion

Xiaoning Guo, Pascal Brault, Guojuan Zhi, Amaël Caillard, Guoqiang Jin, Christophe Coutanceau, Steve Baranton, Xiangyun Guo

Synergistic Combination of Plasma Sputtered Pd-Au Bimetallic Nanoparticles for Catalytic Methane Combustion

Xiaoning Guo [a,c], Pascal Brault [b,*] Guojuan Zhi [a,c], Amaël Caillard [b], Guoqiang Jin [a], Christophe Coutanceau [d], Steve Baranton [d], Xiangyun Guo [a,*],

[a] State Key Laboratory of Coal Conversion, Institute of Coal Chemistry, Taiyuan 030001, PR China

[b] GREMI UMR6606 CNRS - Université d'Orléans BP6744, 45067 ORLEANS Cedex2, France

[c] Graduate University of the Chinese Academy of Sciences, Beijing 100039, PR China

[d] LACCO, UMR6503 CNRS-Université de Poitiers, 40 avenue du Recteur Pineau, 86022 Poitiers, France

*Corresponding author:

Fax/Tel: +86-351 4065282

Email: xyguo@sxicc.ac.cn (X. Y. Guo)

Fax: +33- 2 38 41 71 54; Tel: +33- 2 38 41 71 25

Email: Pascal.Brault@univ-orleans.fr (P. Brault)

Abstract

Pd-Au bimetallic nanoparticles supported by silicon carbide have been prepared by plasma sputtering deposition, and employed as the catalyst for methane combustion. It is found that the bimetallic nanoparticles consist of tight-coupled Pd and Au particles, which are neither Pd-Au alloyed nor core-shell structured. The catalytic activity increases with the Pd loading in the catalysts. When the temperature is higher than 520 ^{o}C, Pd catalysts have an obvious drop in the catalytic activity due to the decomposition of PdO. However the introduction of Au can delay and weaken the drop. It is indicated that there exists a synergistic combination between Pd and Au − oxygen transfers from Pd to Au at the temperature lower than 520 ^{o}C and from Au to Pd at higher temperature. Transmission electron microscopy and X-ray photoelectron spectroscopy results further confirm the synergistic combination.

Keywords: Pd-Au bimetallic catalysts; synergistic combination; methane combustion, plasma sputtering deposition.

1. Introduction

Bimetallic nanoparticles have been known and exploited for many years in various catalytic reactions because catalytic performance, activity, selectivity, and stability can be enhanced compared to corresponding monometallic catalysts due to the synergistic combination of two metals[1,2]. Pd-Au bimetallic catalysts are particularly important because of their widespread applications in important industrial reactions, such as alcohol oxidation, H_2O_2 synthesis and toluene oxidation etc.[3-8]. Usually, the addition of Au can stabilize Pd components, lower the desorption temperature of reaction products and change the nature of active sites. Geometric, electronic and bifunctional effects have been proposed to explain the improvement of catalyst performance[9-11]. However the influences of bimetallic structure and composition on the synergistic combination are still debated by researchers.

Various preparation techniques, such as coimpregnation, coprecipitation and fractional deposition etc., have been proposed for preparation of Pd-Au bimetallic catalysts. However the composition, morphology, and electronic structure of bimetallic nanoparticles are markedly affected by preparation methods and experimental conditions. Recently, plasma sputtering has been studied extensively since the technique is feasible and no post-treatment is needed[12,13]. Most of these studies are related to production of ultra-fine monometallic particles and thin films, direct catalyst deposition on a support or assistance of catalytic reactions[14-16]. Many studies are devoted to preparation of bimetallic nanoparticles[17-18], suggesting that

plasma sputtering has obvious advantages in controlling the composition of bimetallic nanoparticles.

Catalytic combustion of lean natural gas and air mixture has attracted considerable attentions because the process operates at low temperature and produces little NO_x emission[19-23]. The formulation of catalysts can be divided in low and high temperature catalysts which correspond to different stages in the catalytic combustion reactor. Supported palladium catalysts are usually used in the low temperature stage (400-900 ^oC) to initiate methane[24-26]. However, the poor durability of Pd-based catalysts due to decomposition of PdO to Pd limits the development of catalytic combustion of methane[27,28].

In this work, we prepared silicon carbide supported Pd-Au bimetallic nanoparticles using plasma sputtering technique and investigated the structure and composition of the bimetallic nanoparticles by transmission electron microscopy and X-ray photoelectron spectroscopy. The catalytic performance of the bimetallic nanoparticle catalysts for methane combustion indicates that there exists a synergistic combination between Pd and Au components.

2. Experiments

2.1 Catalyst Preparation

Au and Pd sputtering depositions are performed in a cylindrical stainless steel low pressure transformed coupled plasma device. The experimental setup dedicated to the study of metal cluster growth has been described elsewhere[13,29,30]. Briefly, argon plasma is created in a chamber using a planar external RF antenna (13.56 MHz,

300W). The substrate used in this work is high surface area SiC[31,32], which is prepared from a sol–gel and carbothermal reduction route and has a specific surface area of 50.8 $m^2 g^{-1}$ and a pore volume of 0.13 $m^3 g^{-1}$. The plasma depositions were performed under P = 0.5 Pa and V_b = -200 V, where P is the Ar pressure (the base pressure is 5×10^{-5} Pa) and V_b is the bias voltage of pure Au or Pd targets. The deposition time for Au and Pd is 7.5 minutes and 15 minutes, and corresponding samples are marked as $Au_{0.6}$/SiC and $Pd_{0.6}$/SiC, where the subscript represents the metal loading. For preparing $Pd_{0.4}Au_{0.2}$/SiC, the first step is 2.25 minutes for Au deposition and then 10.5 minutes for Pd deposition. For $Pd_{0.2}Au_{0.4}$/SiC, the first step is 4.5 minutes for Pd deposition and then 5.25 minutes for Au deposition.

2.2 Catalytic test

The catalytic performance of different catalysts for the methane combustion was carried out in a fixed-bed quartz reactor with an inner diameter of 8 mm at atmospheric pressure, and the mixture of O_2(20%)/CH_4(1%)/N_2(79%) was used as the feedstock. 140 mg of the catalyst was packed between two layers of quartz wool. The hourly space velocity was controlled to be 12500 h^{-1}. Since the deactivation of the SiC-supported catalysts usually demands a long time, a repeated heating-then-cooling cycle method was employed to estimate the stability of different catalysts as previously reported[33,34].

2.3 Catalyst characterization

The loadings of different metals in the catalysts were determined by Perkin-Elmer ELAN 5000 inductively coupled plasma-mass spectroscopy (ICP-MS) instrument and

energy dispersive spectroscopy (EDS). The microstructures of the catalysts were analyzed by using JEM-2010 high-resolution transmission electron microscope (HRTEM). X-ray photoelectron spectroscopies (XPS) of different catalysts, which were taken at different temperatures in the catalytic combustion of methane, were measured on an ESCALAB 3 MKII de VG spectrometer by using Mg Kα (15kV, 20mA) X-ray source.

3 Results and discussion

3.1 Catalytic performances

The Au and Pd loadings determined by ICP-MS and EDS are listed in table 1. It can be seen that there exists subtle distinctions between the results from ICP-MS and EDS. Because the results from ICP-MS are more accurate, we employ them to represent the metal loadings. For example, in the catalyst $Pd_{0.4}Au_{0.2}$/SiC, the loadings of Pd and Au are 0.4% and 0.2%, respectively.

Fig. 1 shows the reaction results of methane combustion on SiC and $Au_{0.6}$/SiC. Usually the lowest fire point of CH_4 is around 580 ^oC in air. In our experiments, CH_4 could be ignited at 660 ^oC without any catalyst (only SiC), and the conversion could reach to 75% at 760 ^oC (Fig. 1a). However the selectivities of CO_2 and CO are around 60% and 30%, respectively (Fig. 1b and 1c). In other words, the combustion of methane is not complete at the experimental temperature if no metallic catalysts. When employing $Au_{0.6}$/SiC as the catalyst, methane can be converted to CO_2 with a selectivity of 100% at above 660 ^oC and the methane conversion can reach up to 100% at 760 ^oC (Fig. 1d and 1e). The above results indicate that Au supported on

non-oxide materials also has a good catalytic activity for CH_4 combustion at high temperature. The role of Au here is similar to that in CO oxidation. When the system temperature is higher than 660 ^oC, methane is ignited and converted into CO_2, CO and unburned hydrocarbons. The Au nanoparticles dispersed on SiC can dissociate O_2 and produce dissociated oxygen species, which can oxidize CO and unburned hydrocarbons to CO_2. Therefore the CO_2 selectivity on $Au_{0.6}$/SiC can get to 100%.

Fig. 2 shows the methane conversions on different Pd-based catalysts. From Fig. 2a, the methane conversion on $Pd_{0.6}$/SiC increases with the reaction temperature in a relatively low temperature range. When the temperature is higher than 520 ^oC, however the methane conversion begins to decline. It is widely considered that the active phase of Pd-based catalysts in methane combustion is PdO and the declination is due to decomposition of PdO into Pd[27,28]. When employing bimetallic Pd-Au catalysts, it means that partial Pd component in $Pd_{0.6}$/SiC is replaced by Au. Therefore, the activities of Pd-Au catalysts decrease obviously, as shown in Fig. 2b and 2c. It is worth noting that both the activities of $Pd_{0.4}Au_{0.2}$/SiC and $Pd_{0.2}Au_{0.4}$/SiC are higher than that of $Pd_{0.6}$/SiC below 370 ^oC. This indicates that there may have a synergistic effect between Pd and Au components. In addition, the activities of $Pd_{0.4}Au_{0.2}$/SiC and $Pd_{0.2}Au_{0.4}$/SiC begin to decline at 560 ^oC and 580 ^oC, respectively. Both of them are higher than that of $Pd_{0.6}$/SiC (520 ^oC), indicating that the introduction of Au component can delay the declination temperature of Pd-based catalysts. Moreover, the decrements in the catalytic activity (methane conversion) are also less than that using

$Pd_{0.6}$/SiC. These results suggest that the existence of Au could effectively hinder the decomposition of PdO to Pd at higher temperatures.

Methane conversions over the three Pd-based catalysts can reach to 100% at the temperature higher than 760 ^{o}C. Such low loadings of Pd in the Pd-Au bimetallic catalysts, 0.4% and 0.2%, can exhibit a catalytic activity as high as that of $Pd_{0.6}$/SiC, indicating that the Au component has played an important role in the catalytic reaction.

Fig. 3a and 3b show the stabilities of $Pd_{0.4}Au_{0.2}$/SiC and $Pd_{0.2}Au_{0.4}$/SiC catalysts in the combustion of methane. Both catalysts can get to a 100% conversion at 760 ^{o}C, which can remain unchanged after 10 reaction cycles. These indicate that the SiC supported catalysts have excellent stability for the catalytic combustion of methane and the high surface area SiC as the support can effectively stabilize Pd, Au and Pd-Au bimetallic nanoparticles.

3.2 HRTEM characterization

Fig.4 shows HRTEM images of fresh and used $Pd_{0.6}$/SiC catalysts. The used catalysts have completed 10 reaction cycles at 500 ^{o}C, 560 ^{o}C and 730 ^{o}C respectively. The lattice spacings of nanoparticles are around 0.224 and 0.282 nm, which are indexed as (111) planes of Pd and (200) planes of PdO, respectively. Fig. 4a shows that Pd component in the fresh catalyst is metallic palladium, which results from the difference of plasma sputtering deposition and traditional coimpregnation or coprecipitation preparations. Fig.4b indicates that metallic Pd nanoparticles have been completely oxidized into PdO at 500 ^{o}C. From the HRTEM images shown in Fig. 4c

and 4d, only metallic Pd particles can be found instead of PdO. These indicate that PdO can gradually decompose into Pd as the temperature is raised.

Fig.5 and Fig.6 show HRTEM images of fresh and used $Pd_{0.4}Au_{0.2}$/SiC and $Pd_{0.2}Au_{0.4}$/SiC catalysts, which have completed 10 reaction cycles at 560 ^{o}C, 600 ^{o}C and 760 ^{o}C, respectively. In these figures, the lattice spacings of nanoparticles are around 0.235, 0.224, and 0.282 nm, which correspond to (111) planes of Au, (111) planes of Pd, and (200) planes of PdO, respectively. From Fig.5 and Fig.6, it is obvious that the bimetallic nanoparticles consist of tight-coupled Au and Pd particles and they are neither Pd-Au alloyed nor core-shell structured. There are obvious interfaces between Au and Pd components. From these images, the Au component always exists as the metallic phase whatever the temperature is. Contrarily, the Pd component undergoes a transformation of metal-oxide-metal along with the temperature variation. The transformation is mainly due to the oxidation of metallic Pd at low temperature and the decomposition of PdO at high temperature. In the image shown in Fig. 4c, metallic Pd particles can be easily found from used $Pd_{0.6}$/SiC catalyst, indicating that PdO has decomposed into metallic Pd at 560 ^{o}C. However PdO particles are still in the majority in the used bimetallic catalysts even though they have run at 600 ^{o}C for a long time (Fig.5c and Fig.6c). From table 1 and the HRTEM images, the average sizes of metal nanoparticles in all catalysts only have a slight increase after 10 reaction cycles, indicating that high surface area SiC based catalysts have excellent stabilities.

3.3 XPS characterization

Table 2 gives the results of XPS measurements. From table 2, Au 4f binding energy (BE) value at around 83.8 eV can be attributed to Au^0 charge state[35], suggesting that Au can exist as metallic phase at any temperature. Combining with the catalytic performance of $Au_{0.6}$/SiC, the results of XPS further confirm that nanoscale Au particles have high-temperature activity for the catalytic combustion of methane even though they are supported by non-oxide materials such as SiC. Pd $3d_{5/2}$ lines exhibit two peaks at BE values ranging in 334.7-335.1 eV and 337.6-337.8 eV, which can be attributed to Pd^0 and Pd^{2+}, respectively[36-38]. The O 1s BE value at about 529.1 eV is attributed to the lattice oxygen associated with metal oxides, while the O 1s BE value at about 531.6 eV is attributed to absorbed oxygen[39]. Comparing the fresh and used Pd-based catalysts at low temperatures (500 and 560 ^oC), it can be seen from Table 2 and Fig.7 that the concentrations of Pd^{2+} and lattice oxygen increase while the concentrations of absorbed oxygen decreases. The reason is due to the oxidation of metallic Pd in the reaction. For the Pd catalysts used at higher temperatures, the concentration of above three species change in opposite direction mainly due to the decomposition of PdO. Although the concentrations of Pd^{2+} and lattice oxygen gradually decrease at high temperatures, both the decrements in $Pd_{0.4}Au_{0.2}$/SiC and $Pd_{0.2}Au_{0.4}$/SiC are less than the Au-free Pd catalyst. Moreover, the more Au content is in the Pd-Au catalysts, the less the Pd^{2+} content decreases.

The above results indicate that Pd-Au bimetals in the catalytic process have synergistic effect apart from the specific performances of themselves. This can be

interpreted by a simple model about the transference of dissociated oxygen species between Pd and Au during the reaction.

(a) At the temperature below 500 ^{o}C, O_2 can be dissociated and chemically adsorbed on Pd nanoparticles and form into PdO. The formation rate of PdO increases rapidly with the temperature increasing. Meanwhile, the dissociation rate of O_2 is much higher than the chemical adsorption rate of dissociated oxygen species on Pd. And thus the concentration of dissociated oxygen species on Pd increases quickly. The additional oxygen species transfer from Pd to Au through interfaces of Pd and Au, and Au here plays a role of reservoir for dissociated oxygen. As a result, the equilibrium favors the direction of O_2 dissociation.

(b) PdO starts to decompose into Pd and O_2 when the temperature is above 520 ^{o}C. The decomposition rate of PdO becomes higher than the dissociation and chemical adsorption rate of O_2. At this time, dissociated oxygen species transfer from the Au reservoir to Pd through Pd and Au interfaces because the metallic activity of Pd is higher than that of Au. As a result, PdO as the active phase for methane combustion can keep relatively high concentration.

(c) At high temperature, e.g. above 660 ^{o}C, O_2 is dissociated and chemically adsorbed on Au nanoparticles due to the high-temperature activity[40]. The dissociated oxygen species on Au transfer to Pd through interfaces of Pd and Au. Therefore, both Pd and Au in the bimetallic catalysts can catalyze the combustion of methane through the synergistic combination.

4. Conclusion

Silicon carbide supported Pd-Au bimetallic nanoparticles were prepared by plasma sputtering deposition. The bimetallic particles have a tight-coupled structure. It is found that the introduction of Au can improve the catalytic performance of Pd-based catalysts for the catalytic combustion of methane. The improvement results from the synergistic combination between Pd and Au nanoparticles. At different reaction temperatures, the Au component plays roles of reservoir and provider of dissociated oxygen species, respectively. The average sizes of nanoparticles of all the SiC-based catalysts only have a slight increase suggesting that high surface area SiC could effectively hinder the migration and sintering of metal nanoparticles.

Acknowledgments

The work was financially supported by NSFC (Ref. 20973190), the in-house research project of SKLCC (Ref. SKLCC-2008BWZ010), and the National Basic Research Program (Ref. 2011CB201405).

References

(1) Fang, Y. L.; Miller, J. T .; N. Guo, Heck, K. N.; Alvarez, P. J. J.; Wong, M. S. *Catal. Today* **2011**, *160*, 96-102.

(2) Molenbroek, A. M.; Haukka, S.; Clausen, B. S. *J. Phys. Chem. B* **1998**, *102*, 10680-10689.

(3) Enache, D. I., Edwards, J. K., Landon, P., Solsona-Espriu, B., Carley, A. F., Herzing, A. A., Watanabe, M., Kiely, C. J., Knight, D. W., Hutchings, G. J. *Science* **2006**, *311*, 362-365.

(4) Edwards, J. K., Solsona, B., Ntainjua N, E., Carley, A. F., Herzing, A. A., Kiely, C.

J., Hutchings, G. J. *Science* **2009**, *323*, 1037-1041.

(5) Kesavan, L., Tiruvalam, R., Rahim,M. H., Saiman, M. I., Enache, D. I., Jenkins, R. L., Dimitratos, N., Lopez-Sanchez, J. A., Taylor, S. H., Knight, D. W., Kiely, C. J., Hutchings, G. J. *Science* **2011**, *331*, 195-199.

(6) Wei, T.; Wang, J. H.; Goodman, D. W. *J. Phys. Chem. C* **2007**, *111*, 8781-8788.

(7) Li, G.; Edwards, J.; Carley, A. F.; Hutchings, G. J. *Catal. Today* **2007**, *122*, 361-364.

(8) Edwards, J. K.; Thomas, A.; Carley, A. F.; Herzing, A. A.; Kiely, C. J.; Hutchings, G. J. *Green Chem.* **2008**, *10*, 388-394.

(9) Chen, M. S.; Kumar, D. C.; Yi, W.; Goodman, D. W. *Science* **2005**, *310*, 291-293.

(10) Maroun, F.; Ozanam, F.; Magnussen, O. M.; Behm, R. J. *Science* **2001**, *293*, 1811-1814.

(11) Ponec, V. *Appl. Catal. A.* **2001**, *222*, 31-45.

(12) Chen, Q.; Zhang, Y. F.; Yang, L. Z.; Chen, S. G.; Weng, J.; Yue, L. *J. Phys. Chem. C* **2009**, *113*, 7633-7638.

(13) Rabat, H.; Andreazzac, C.; Brault, P.; Caillard, A.; Béguin, F.; Charles, C.; Boswell, R. *Carbon* **2009**, *47*, 209-214.

(14) Berthet, A.; Thomann, A. L.; Cadete Santos Aires, F. J.; Brun, M.; Deranlot, C.; Bertolini, J. C.; Rozenbaum, J. P.; Brault, P.; Andreazzaz, P. *J. Catal.* **2000**, *190*, 49-59.

(15) Xie, M.; Wang, J. S.; Khin Yap, Y. *J. Phys. Chem. C* **2010**, *114*, 16236-16241.

(16) Sonoda, T.; Watazu, A.; Zhu, J.; Kamiya, A.; Nonami, T.; Kameyama, T.;

Naganuma, K.; Kato, M. *Thin Solid Films* **2001**, *386*, 227-232.

(17) Zhang, H. X.; Wang, C.; Wang, J. Y.; Zhai, J. J.; Cai, W. B. *J. Phys. Chem. C* **2010**, *114*, 6446-6451.

(18) Ito, Y.; Miyazaki, A.; Valiyaveettil, S.; Enoki, T. *J. Phys. Chem. C* **2010**, *114*, 11699-11702.

(19) Ciuparu, D.; Lyubovsky, M. R.; Altman, E.; Pfefferle, L. D.; Datye, A. *Catal. Rev.* **2002**, *44*, 593-649.

(20) Gélin, P.; Primet, M. *Appl. Catal. B* **2002**, *39*, 1-37.

(21) Zwinkels, M. F. M.; Järås, S. G.; Menon, P. G.; Griffin, T. A. *Catal. Rev.* **1993**, *35*, 319-358.

(22) Trimm, D. L. *Appl. Catal.* **1983**, *7*, 249-282.

(23) Quick, L. M.; Kamitomai, S. *Catal. Today* **1995**, *26*, 303-308.

(24) Pfefferle, L. D.; Pfefferle, W. C. *Catal. Rev.* **1987**, *29*, 219-267.

(25) Arai, H.; Fukuzawa, H. *Catal. Today* **1995**, *26*, 217-221.

(26) Euzen, P.; Le Gal, J. H.; Rebours, B.; Martin, G. *Catal. Today* **1999**, *47*, 19-27.

(27) Farrauto, R. J. ; Hobson, M. C. ; Kennelly, T.; Waterman, E. M. *Appl. Catal. A* **1992**, *81*, 227-237.

(28) Ozawa, Y.; Tochihara, Y.; Nagai, M.; Omi, S. *Chem. Eng. Sci.* **2003**, *58*, 671-677.

(29) Rabat, H.; Brault, P. *Fuel Cells* **2008**, *8*, 81-86.

(30) Thomann, A. L.; Brault, P.; Rozenbaum, J. P.; Andreazza-Vignolle, C.; Andreazza, P.; Estrade-Szwarckopf, H.; Rousseau, B.; Babonneau,D.;

Blondiaux,G. *J. Phys. D: Appl. Phys.* **1997**, *30*, 3197-3202.

(31) Jin, G. Q.; Guo, X. Y. *Micropor. Mesopor. Mat.* **2003**, *60*, 207-212.

(32) Guo, X. Y.; Jin, G. Q. *J. Mater. Sci.* **2005**, *40*, 1301-1303.

(33) Guo, X. N.; Shang, R. J.; Wang, D. H.; Jin, G. Q.; Guo, X. Y.; Tu, K. N. *Nanoscale Res. Lett.* **2010**, *5*, 332-337.

(34) X Guo,. N.; Zhi, G. J.; Yan, X. Y.; Jin, G. Q.; Guo, X. Y.; Brault, P. *Catal. Commun.* **2011**, *12*, 870-874.

(35) Choudhary, V. R.; V Patil,. P.; Jana, P.; Uphade, B. S. *Appl. Catal. A* **2008**, *350*, 186-190.

(36) Nelson, A. E. ; Schulz, K. H. *Appl. Surf. Sci.* **2003**, *210*, 206-221.

(37) Galtayries, A.; Sporken, R.; Riga, J.; Blanchard, G.; Caudano, R. *J. Electron Spectrosc. Rel. Phen.* **1998**, *88*, 951-956.

(38) Arai, H.; Machida, M. *Catal. Today* **1991**, *10*, 81-94.

(39) Wang, S. P.; Zheng, X. C.; Wang, X. Y.; Wang, S. R.; Zhang, S. M.; Yu, L. H.; Huang, W. P.; Wu, S. H. *Catal. Lett.* **2005**, *105*, 163-168.

(40) Grisel, R. J. H.; Kooyman, P. J.; Nieuwenhuys, B. E. *J. Catal.* **2000**, *191*, 430-437.

Tables

Table 1 Au and Pd loading of different catalysts and the average size of nanoparticles of different fresh and used catalysts.

Samples	Au loading (wt.%)		Pd loading (wt.%)		Nanopaticle size (HRTEM) (nm)	
	ICP-MS	EDS	ICP-MS	EDS	Fresh catalyst	Used catalyst (after 10 cycles)
$Au_{0.6}$/SiC	0.61	0.54	—	—	4.17	4.89
$Pd_{0.6}$/SiC	—	—	0.63	0.52	3.74	4.86
$Pd_{0.4}Au_{0.2}$/SiC	0.19	0.13	0.42	0.39	5.12	6.03
$Pd_{0.2}$/$Au_{0.4}$SiC	0.40	0.36	0.22	0.15	4.01	5.34

Samples	O 1s (O-metal)		Au 4f	Pd 3d	
	lattice oxygen BE (eV)[a]	adsorbed oxygen BE (eV)	BE (eV)	Pd^0 BE (eV)	Pd^{2+} BE (eV)
$Au_{0.6}$/SiC(fresh)	529.1 (4.3)[b]	531.6 (95.7)	83.8	—	—
$Au_{0.6}$/SiC(760°C)[c]	529.1 (3.2)	531.5 (96.8)	84.0	—	—
$Pd_{0.6}$/SiC(fresh)	529.0 (5.1)	531.5 (94.9)	—	334.7 (96.7)[d]	337.7 (3.3)
$Pd_{0.6}$/SiC(500°C)	529.1 (67.9)	531.7 (32.1)	—	334.7 (6.4)	337.8 (93.6)

$Pd_{0.6}$/SiC(560°C)	529.0 (51.5)	531.6 (48.5)	—	335.0 (21.9)	337.6 (78.1)
$Pd_{0.6}$/SiC(730°C)	529.2 (29.8)	531.7 (70.2)	—	334.8 (34.6)	337.6 (65.4)
$Pd_{0.4}Au_{0.2}$/SiC(fresh)	529.1 (3.4)	531.6 (96.6)	83.8	334.9 (95.4)	337.6 (4.6)
$Pd_{0.4}Au_{0.2}$/SiC(560°C)	529.0 (48.6)	531.6 (51.4)	83.9	334.7 (5.1)	337.8 (94.9)
$Pd_{0.4}Au_{0.2}$/SiC(600°C)	529.0 (41.1)	531.5 (58.9)	83.9	334.8 (15.7)	337.6 (84.3)
$Pd_{0.4}Au_{0.2}$/SiC(760°C)	529.1 (37.4)	531.7 (62.6)	84.0	334.7 (23.3)	337.6 (76.7)
$Pd_{0.2}Au_{0.4}$/SiC(fresh)	529.1 (5.0)	531.6 (95.0)	83.9	334.8 (96.2)	337.7 (3.8)
$Pd_{0.2}Au_{0.4}$/SiC(560°C)	529.1 (33.9)	531.6 (66.1)	84.0	334.9 (3.5)	337.8 (96.5)
$Pd_{0.2}Au_{0.4}$/SiC(600°C)	529.1 (26.1)	531.5 (73.9)	84.0	334.7 (11.2)	337.7 (88.8)
$Pd_{0.2}Au_{0.4}$/SiC(760°C)	529.0 (21.3)	531.7 (78.7)	84.0	334.9 (19.4)	337.7 (80.6)

Table 2 Binding energies (eV) of Au 4f and Pd 3d of different fresh and used catalysts which were taken at different temperatures in the CH_4 methane catalytic combustion reaction.

a The binding energy (BE) values were corrected using the C1s peak at 285.0 eV.

b The value in the brackets refers to the relative content of the components of the O 1s (O-metal) spectra.

c The characterized samples were taken at the 760°C in the methane catalytic combustion reaction.d The value in the brackets refers to the relative content of the components of the Pd 3d spectra.

Figures captions:

Fig.1 CH_4 conversion and CO_2 selectivity of SiC and $Au_{0.6}$/SiC for methane combustion.

Fig.2 Catalytic activities of $Pd_{0.6}$/SiC, $Pd_{0.4}Au_{0.2}$/SiC and $Pd_{0.2}Au_{0.4}$/SiC for methane combustion.

Fig.3 Catalytic stabilities of $Pd_{0.4}Au_{0.2}$/SiC (a) and $Pd_{0.2}Au_{0.4}$/SiC (b) for methane

combustion.

Fig.4 HRTEM images of fresh (a) and used $Pd_{0.6}$/SiC catalysts which were taken at 500^{o}C (b), 560^{o}C (c) and 730^{o}C (d) respectively in the CH_4 methane catalytic combustion reaction; and the size distribution of the nanoparticles.

Fig.5 HRTEM images of fresh (a) and used $Pd_{0.4}Au_{0.2}$/SiC catalysts which were taken at 560^{o}C (b), 600^{o}C (c) and 760^{o}C (d) respectively in the CH_4 methane catalytic combustion reaction; and the size distribution of the nanoparticles.

Fig.6 HRTEM images of fresh (a) and used $Pd_{0.2}Au_{0.4}$/SiC catalysts which were taken at 560^{o}C (b), 600^{o}C (c) and 760^{o}C (d) respectively in the CH_4 methane catalytic combustion reaction; and the size distribution of the nanoparticles.

Fig.7 XPS spectra of O 1s of $Pd_{0.6}$/SiC, $Pd_{0.4}Au_{0.2}$/SiC and $Pd_{0.2}Au_{0.4}$/SiC which were taken at different temperature (before and after deactivation of catalysts.

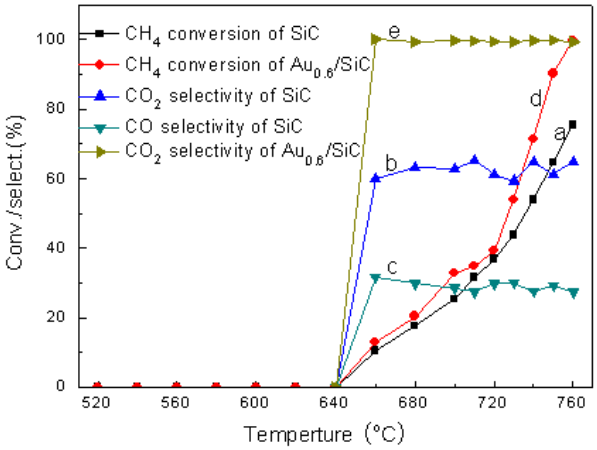

Fig.1 CH_4 conversion and CO_2 selectivity of SiC and $Au_{0.6}$/SiC for methane combustion.

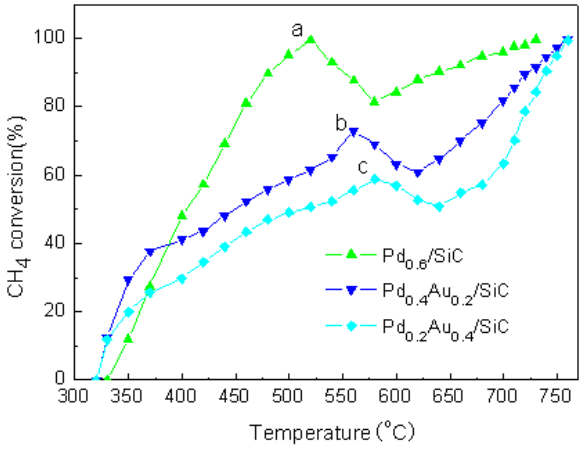

Fig.2 Catalytic activities of $Pd_{0.6}$/SiC, $Pd_{0.4}Au_{0.2}$/SiC and $Pd_{0.2}Au_{0.4}$/SiC for methane combustion.

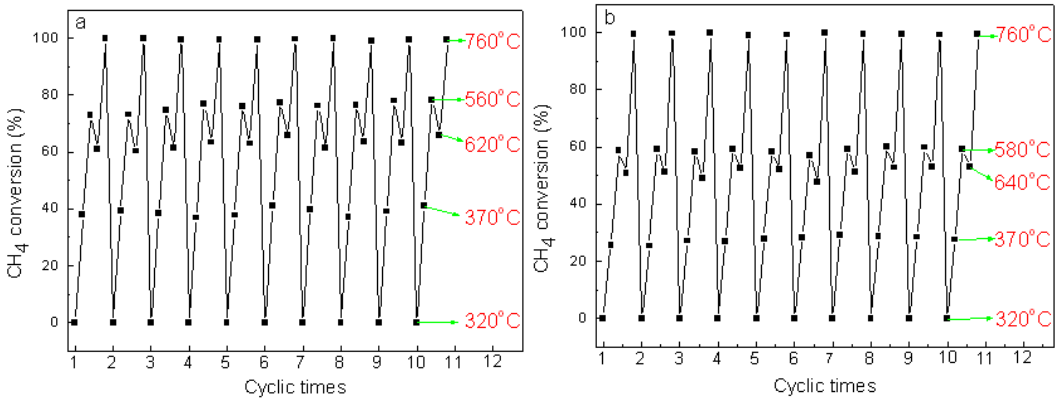

Fig.3 Catalytic stabilities of $Pd_{0.4}Au_{0.2}$/SiC (a) and $Pd_{0.2}Au_{0.4}$/SiC (b) for methane combustion.

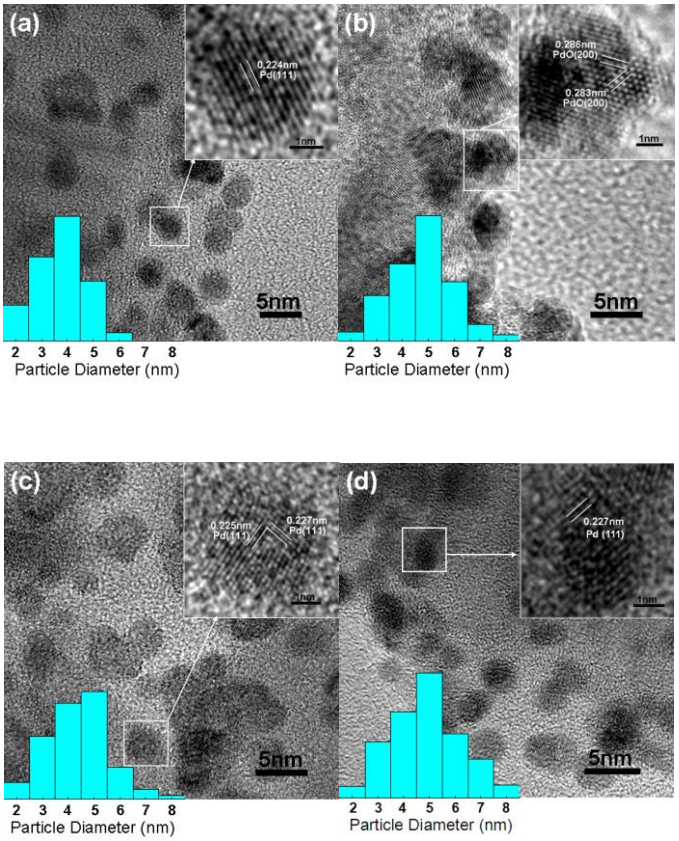

Fig.4 HRTEM images of fresh (a) and used $Pd_{0.6}$/SiC catalysts which were taken at 500^{o}C (b), 560^{o}C (c) and 730^{o}C (d) respectively in the CH_4 methane catalytic combustion reaction; and the size distribution of the nanoparticles.

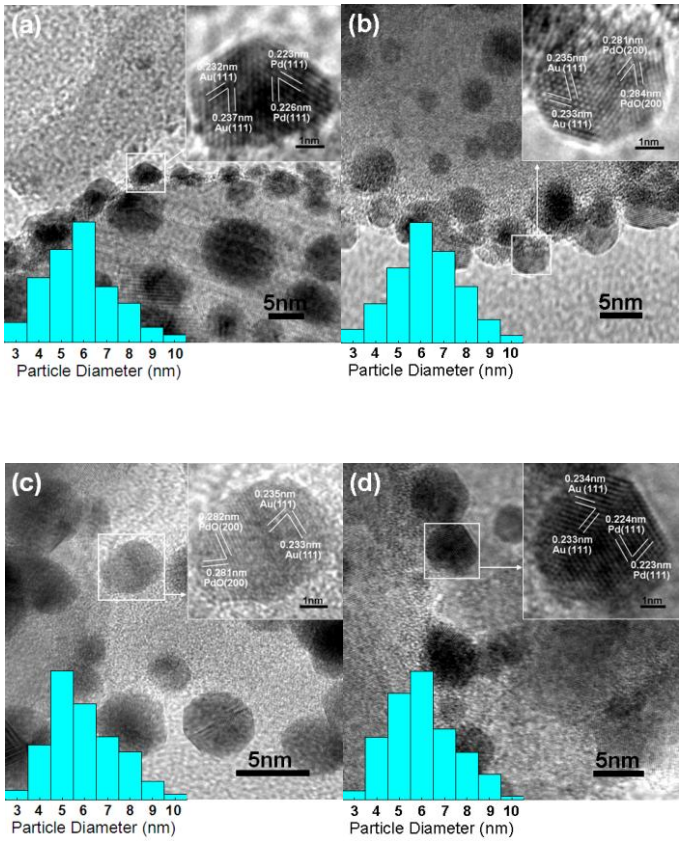

Fig.5 HRTEM images of fresh (a) and used $Pd_{0.4}Au_{0.2}$/SiC catalysts which were taken at 560^{o}C (b), 600^{o}C (c) and 760^{o}C (d) respectively in the CH_4 methane catalytic combustion reaction; and the size distribution of the nanoparticles.

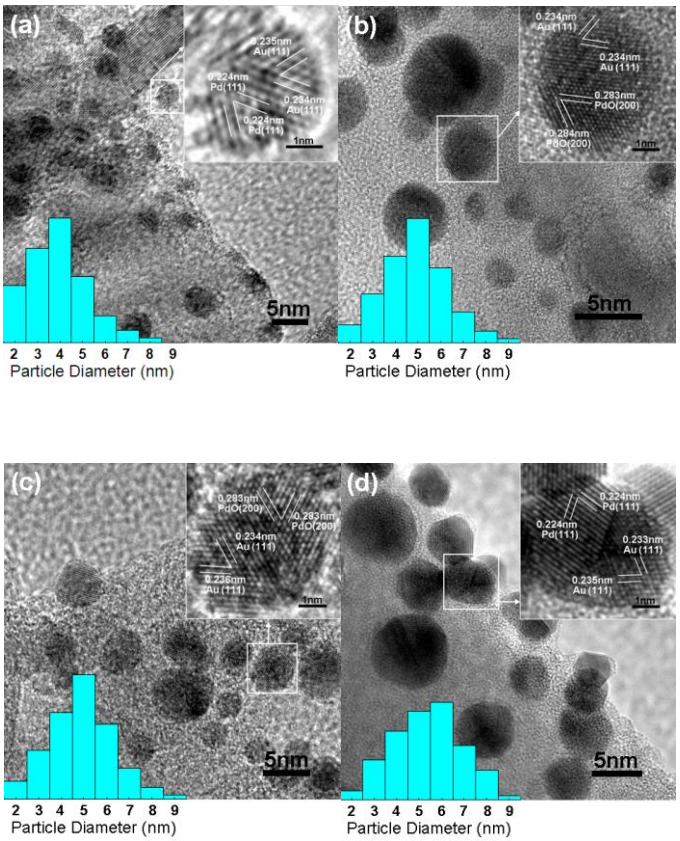

Fig.6 HRTEM images of fresh (a) and used $Pd_{0.2}Au_{0.4}$/SiC catalysts which were taken at 560°C (b), 600°C (c) and 760°C (d) respectively in the CH_4 methane catalytic combustion reaction; and the size distribution of the nanoparticles.

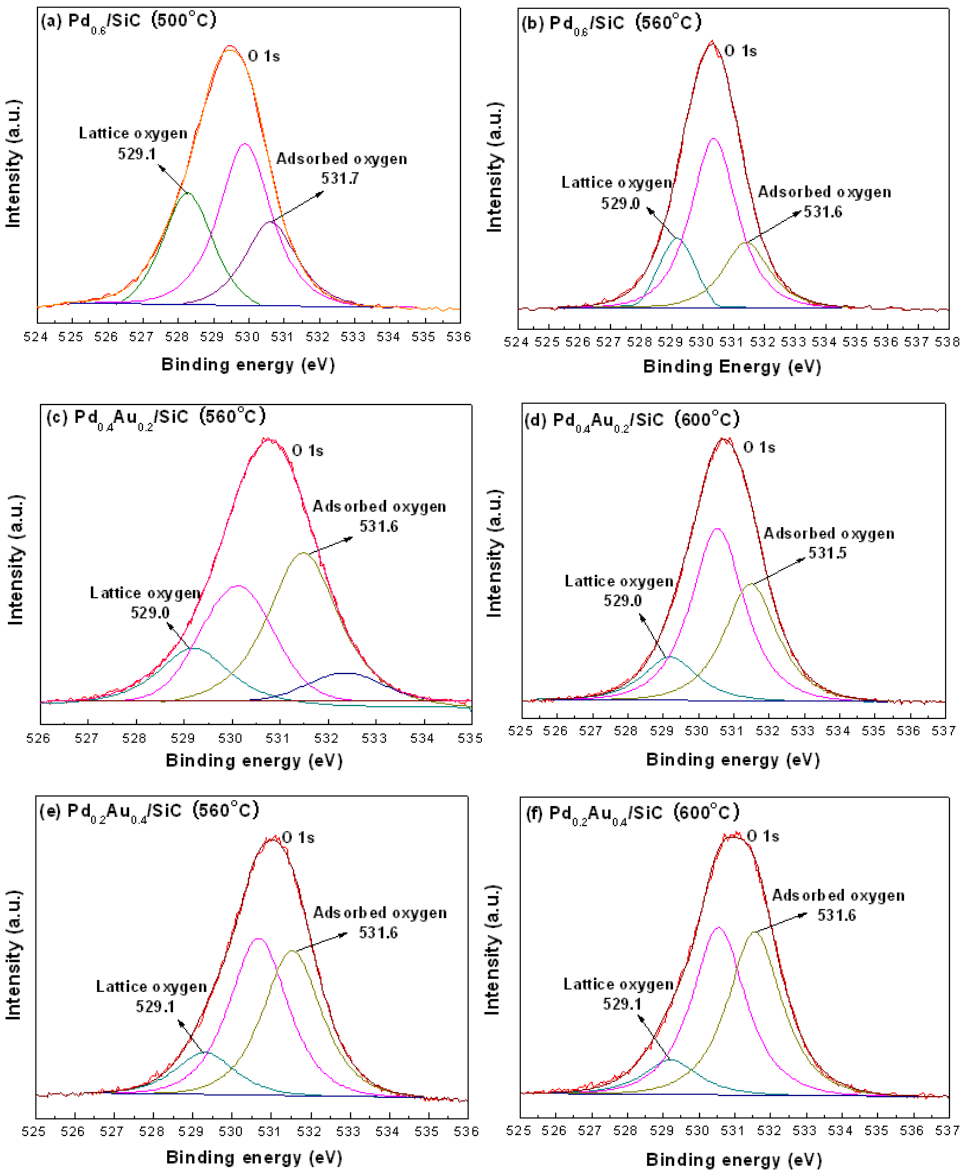

Fig.7 XPS spectra of O 1s of $Pd_{0.6}$/SiC, $Pd_{0.4}Au_{0.2}$/SiC and $Pd_{0.2}Au_{0.4}$/SiC catalysts at different temperatures.